CHAPTER 3

Room Temperature Crystal Structure of (1-x)Ba($Cu_{1/3}Nb_{2/3}$)O_3-(x)$PbTiO_3$ Ceramics

CHAPTER 3.

Room Temperature Crystal Structure of (1-x)Ba($Cu_{1/3}Nb_{2/3}$)O_3-(x)$PbTiO_3$ Ceramics

3.1 Introduction

The simultaneous existence of two different crystal structures, observed in so-called monophasic oxide compounds, is generally found at the phase boundaries of the solid solutions and in some Cu and Mn-based metal oxide compounds in the form of phase separation [73]. The phase boundary compositions in perovskite solid solutions may possess the simultaneous coexistence of two or more crystallographic phases that may arise due to first order nature of the phase transition and associated nucleation and growth process of the transforming phases. Generally, the coexisting phases in a solid solution are among the borderline parent-daughter phases. Sometimes, an additional low-symmetry phase, such as monoclinic, orthorhombic, etc., may exist to bridge the structural gap between the parent and daughter phases [74,75]. These additional phases mostly arise to satisfy the crystallographic group-subgroup relations when they are not satisfied by the transformation of the parent into the daughter for phase transformations of the first-order kind [33,76].

As discussed in chapter 1, the solid solutions of BCN with BNT, BFO and BT have been explored in the literature and found to possess an MPB for a very small concentration ($x > 0.05$) of BCN. In the solid solution of (1-x)BCN-(x)PT also the same phenomenon have been observed in addition to the other MPB lying at further higher BCN content ($x > 0.50$) that was not explored before our work. As mentioned in chapter 1, only two compositions (0.10)BCN-(0.90)PT and (0.05)BCN-(0.95)PT of the solid solution (1-x)BCN-(x)PT have been briefly investigated for their temperature-dependent dielectric and electromechanical properties by Priya et al. in 2003 [47].

In this chapter, an attempt has been made to investigate the fascinating crystallographic modification in the different compositions of the (1-x)BCN-(x)PT solid solution as a function of composition to correlate it with various possible phenomena, such as thermodynamic phase transformation, phase separation and the presence of multiple phase boundaries. Additionally, a road map for finding crystal structural solutions for previously unknown perovskite systems with mixed phases is also briefly discussed in the beginning of the chapter. A detailed study of the room temperature (RT) crystal structure of the (1-x)BCN-(x)PT solid solution has been done at close compositional interval in the whole composition range. At RT, phase coexistence has been observed in every composition in the range $0.59 \leq x \leq 0.975$, along with the presence of multiple phase boundaries. The temperature-dependent crystal structure evolution of these phases is a subject matter for the next chapter, where these phase boundaries are observed to exhibit morphotropic nature. As far as we know, any similar occurrence of so many phase boundaries and crystal structure evolution in the perovskite oxides has not been reported yet.

3.2 Overview and Preliminary Picture of the phase evolution in (1-x)BCN-(x)PT Ceramics

In this Section, the crystal structural analysis using XRD data on some selected compositions of the (1-x)BCN-(x)PT have been briefly presented to create a preliminary picture of crystal structure evolution with compositional variation. The abbreviation of the compositions is used as ‘x’ number values to identify a particular composition of (1-x)BCN-(x)PT. A total 18 compositions have been studied, viz., x = 0, 0.05, 0.10, 0.20, 0.40, 0.55, 0.59, 0.60, 0.62, 0.65, 0.70, 0.75, 0.80, 0.85, 0.90, 0.95, 0.975 and 1. The XRD patterns of some of the representative distinct structured compositions recorded on high-resolution XRD are shown in Fig 3.1(a). For further illustration of the gradual evolution of crystal structures, a zoomed view of pseudocubic (111) and (200) XRD reflections have been shown in Fig 3.1(b and c).

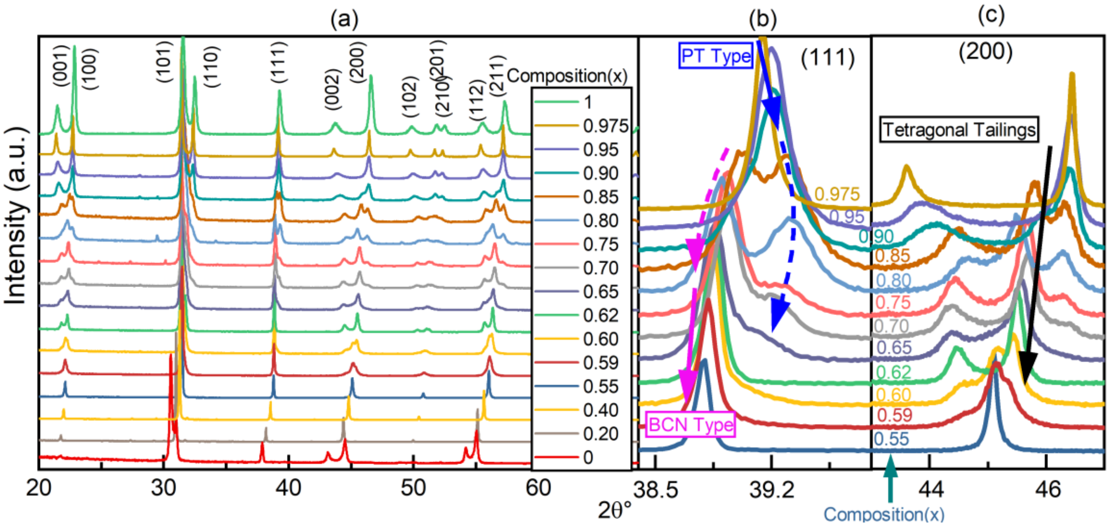

Fig 3.1 (a) HR-XRD pattern of (1-x)BCN-(x)PT solid solution for the composition range $0 \leq x \leq 1$; Zoomed view of pseudocubic (b) (111) and (c) (200) reflection for $0.55 \leq x \leq 0.975$

It can be observed from Fig 3.1(b) that there is a steady shift in the (111) peaks towards the larger 2θ angles as the composition (‘x’ value) increases. The unit cell volume variation can be manifested by the (111) peak positions. A gradual decrement in the unit cell volume with increasing PT content is reflected in the solid solution. The peak position of the pseudocubic (111) reflection of pure BCN appears at 38.1°, which gradually shifts to the higher 2θ angles as ‘x’ increases and appears at 39.44° for pure PT. The compositions with $x > 0.55$ show clear and notable splitting (doublet/triplet) of the (200) reflection as can be seen Fig 3.1(c). This splitting gets more pronounced as composition increases, until it matches the large tetragonal splitting of pure PT.

Likewise, the (111) pseudocubic XRD profile also shows a doublet-like appearance (for 0.80 and 0.85 in Fig 3.1(b)) and an asymmetric hump (for 0.65, 0.70 and 0.75) in the intermediate compositions that can be attributed to the crystallographic phase coexistence.

It is intriguing to note that despite the fact that both the end components of the solid solution are non-centrosymmetric tetragonal, a centrosymmetric cubic structure in the first half ($0.05 \leq x \leq 0.55$) of the solid solution compositions has been observed, similar to many other PT and BT-based solid solutions but with non-tetragonal end components [77,78]. For further higher compositions, the solid solution adopts different crystallographic structures and coexistence regions to accommodate the lattices of BCN-like and PT-like phases, formed by the gradual transformation of modified BCN and modified PT phases (see Fig 3.1(b)). After solid solution formation, extreme compositions in the phase coexistence regions show two different types of tetragonal phases, one resulting from the modification in the BCN-based lattice (designated as T_1) and the other resulting from modification in the PT-based lattice (designated as T_3). Similarly, two different types of monoclinic phases are also observed in the phase coexistence region, one resulting from the BCN-based lattice (designated as M_1) and the other resulting from the PT-based lattice (designated as M_3). In addition, another tetragonal phase (T_2) is observed, resulting from the thermodynamic phase transition of the T_1 phases, originated from BCN-like phases. The BCN-like lattice phases are dominantly present in the composition region $0.20 \leq x \leq 0.62$, whereas the dominance of PT-like lattice phases can be found in the composition region $0.95 \leq x \leq 0.975$ as revealed from the pseudocubic (111) and (200) XRD peak progressions in Fig 3.1(b). The composition region $0.65 < x < 0.90$ shares both kinds of phase, as can be seen from the (111) peak progression (dashed arrows in Fig 3.1(b)). The (200) peak illustrates the lattice distortion accommodation and evolution of BCN and PT-like lattice tetragonal phases of the solid solution as the composition varies (see tetragonal tailings in Fig 3.1(c)]. This kind of structural modification gives rise to unusual kinds of phase coexistence in the solid solution. The phase dynamics of the solid solution is covered in the next chapter in Section 4.5. The details of the crystal structure evolution with contemplation of possible combinative phases for the crystal structural solution have been discussed in the subsection 3.5.

3.3 Path Way for Finding Crystal Structure Solution

Finding the correct crystal structure solution can be complex, especially when two or more phases coexist. It becomes even more challenging if the coexisting phases include any low-symmetry phases. The number of overlapping XRD peaks also grows as the number of possible crystal structural combinations does. One can determine the number of XRD peaks present in an overlapping region by peak deconvolution, followed by identifying the possible crystal structure combinations based on the space group symmetry restrictions. A schematic of the number of reflections/peaks for some commonly encountered crystal systems in typical ferroelectric perovskites, viz. cubic (*Pm*-3*m* space group), tetragonal (*P*4*mm* space group), orthorhombic (*Bmm*2 space group), monoclinic (*Pm* space group), and rhombohedral (*R*3m space group), is shown in Fig 3.2(a). The intensities of the reflections have been estimated based on their multiplicity. Although the positions of the reflections are evenly spaced in Fig 3.2(a) for schematic representations, as a matter of fact, they vary according to the lattice parameter values.

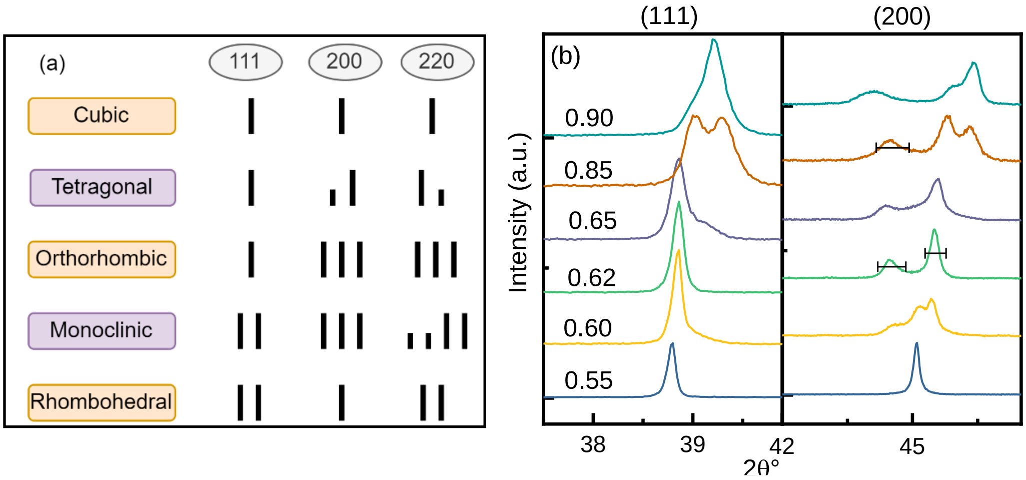

Fig 3.2 (a) Schematic diagram showing characteristic peak splitting of pseudocubic (111), (200) and (220) for perovskite-structured ferroelectric ceramics; (b) HR-XRD (λ = 1.54056Å) pattern of (111) and (200) reflection of the 0.55, 0.60, 0.62, 0.65, 0.85 and 0.90 compositions of (1-x)BCN-(x)PT ceramics

In order to find out the crystal structure of the (1-x)BCN-(x)PT solid solution especially in the phase coexistence region, six representative compositions (0.55, 0.60, 0.62, 0.65, 0.85 and 0.90) were selected that had the most distinct XRD patterns. The (111) and (200) reflections of these compositions are shown in Fig 3.2(b). Based on Fig 3.2(a), an obvious assessment of the crystal systems corresponding to the 0.55, 0.60, and 0.62 compositions is a cubic, a coexisting cubic and tetragonal, and a tetragonal system, respectively. While above the 0.62 composition, multiple peaks in both the (111) and (200) XRD profiles indicate the presence of other coexisting low symmetry phases such as orthorhombic, monoclinic, rhombohedral, etc. Moreover, the (002) peak of the 0.62 composition is unusually broader than (200/020) for a typical single-phase tetragonal structure. Although such broadening can be admirably managed by taking account of thermal parameters and microstructural and anisotropic corrections using a suitable peak profile, it can still be a misleading interpretation in many cases and should not be managed by refinement tactics. Instead, in such cases, a slower scan and/or a higher resolution diffraction pattern recording from monochromatic radiation can aid in an unambiguous determination of the crystal structure. Similarly, the presence of two or more overlapping peaks in each pseudocubic reflection for the compositions 0.60, 0.62, 0.65, 0.85 and 0.90 should be weighted carefully for the determination of crystal structure. This has been carried out by comparing the Rietveld Refinement fits for the plausible crystal structures and coexisting structure combinations, as discussed in subsection 3.5.

3.4 Notations and Nomenclature of Phases in (1-x)BCN-(x)PT Ceramics

As discussed in subsequent sections, the phase coexistence in (1-x)BCN-(x)PT is very complex. For a simplified understanding of phase coexistence and to differentiate between the crystal structures of the phases belonging to a specific composition, certain terminology is assigned by writing the short-forms of their respective crystal systems in a specific sequence. The representations for cubic, tetragonal and monoclinic phases are denoted by their first capital letters such as C, T and M, respectively. For two coexisting phases, the two space groups are separated by a plus (+) symbol in descriptions. It should be noted that, three notations of phases are required to clearly understand the solid solution, depending on how those phases get transformed into other crystallographic phases, while minimizing the structural distortions corresponding to a particular phase. For defining crystal systems for a phase with same space group, the notation is done with the subscripts “1”, “2” and “3” to the initials of the crystal systems respective to phase 1, phase 2 and phase 3. Each phase is an individual representative of one kind (BCN or PT-like) of lattice and transforms into the same or a different crystallographic symmetry based on successive strain accommodations with varying compositions during structural transformations. The vertical tick marks have been used to show the positions of Bragg's reflection and are also arranged in a specific order for their differentiation in multi-phase coexistence in Fig 3.4 to Fig 3.9. Bragg's peak position of a phase having the lowest numbering lies above in all the Rietveld-fitted patterns. For example, in a composition having phase combinations 2 and 3, Bragg's positions for phase 2 is on the upper side and the same for phase 3 lies below.

3.5 Crystal Structure Progression and Illustration of Competing Crystal Structures for (1-x)BCN-(x)PT

For better understanding of the phase evolution, a schematic presentation of the phases and the expected location of phase boundaries is presented in Fig 3.3(a) in advance, before discussing detailed analysis of the structure of the various phases for different compositions of (1-x)BCN-(x)PT solid solution. Fig 3.3(b, c and d) depicts a typical unit cell for the cubic (in 0.55 composition), tetragonal (in 0.85 composition) and monoclinic (in 0.85 composition) structures.

In the composition range $0.05 \leq x \leq 0.55$, the crystal structure is cubic (C_1) with *Pm*-3*m* space group, as can be seen from the singlet nature of the diffraction profiles in Fig 3.1(a). Therefore, a phase boundary exists between $x = 0$ and $x = 0.05$ since pure phase BCN possesses tetragonal symmetry. In the 0.59 composition, there is a coexistence of two phases: phase 1, the cubic structure, similar to that for lower compositions ($0.05 \leq x \leq 0.55$), and phase 2, the tetragonal phase (T_2), which emerges from the thermodynamic phase transition and consequent coexistence. As a result, another phase boundary is expected between the 0.55 and 0.59 compositions of the solid solution. The crystal structure for the composition region $0.59 \leq x \leq 0.60$ is represented by 'C_1+T_2'. After that, phase 1 (C_1) then abruptly changes into a tetragonal phase with

*P*4*mm* space group, while phase 2 remains a similar type, resulting in two coexisting tetragonal phases ('T_1+T_2') in the composition range $0.60 < x \leq 0.62$. Phase 1 (now tetragonal T_1) continues to modify further with increasing PT concentration into a monoclinic phase (M_1) with *Pm* space group for the composition span $0.62 < x \leq 0.65$, resulting in a coexistence of monoclinic and tetragonal phases ('M_1+T_2'). The lattice parameters of the monoclinic structure of the 0.65 composition were close to the 'T_1' structure of the 0.62 composition, while the lattice parameters of the other coexisting tetragonal structure of the 0.65 composition had more similarity in the lattice dimensions of the 'T_2' structure of 0.62 composition. Therefore, the monoclinic structure of the 0.65 composition was designated as 'M_1' instead of 'M_2'. Likewise, the other monoclinic phase has the lattice parameters close to the tetragonal T_3 and therefore designated as M_3. The crystal structures of the 0.65 and 0.70 compositions appear similar, as can be seen from the similar XRD patterns for them, shown in Fig 3.1(a). Both compositions also exhibit the coexistence of monoclinic and tetragonal symmetry. However, contrastively, the Rietveld fits of these compositions revealed that despite having identical combinatory phase types [coexisting tetragonal (*P*4*mm*) and monoclinic (*Pm*)], they do not share the same crystallographic origin of their respective phases because one monoclinic phase (M_1) emerges from a BCN-like lattice, while the other monoclinic phase (M_3) results from a PT-like lattice. This is discussed in detail in subsections 3.5.4 and 3.5.5. Consequently, 2 phase boundaries are located here, one before and one after the 0.65 composition, and their precise location can be discovered by investigating the crystal structure of compositions within close intervals. The crystal structure of the composition in the range of $0.70 \leq x \leq 0.85$ possesses the same crystal structure symmetry, i.e., 'T_2+M_3'. In the 0.90 composition, only monoclinic (M_3) phase 3 transforms to a tetragonal structure (T_3); thus, the crystal structure consists of two coexisting tetragonal phases, both with the *P*4*mm* space group as confirmed from the Rietveld structure refinement. All the compositions between the 0.90 and 0.975 compositions can be represented as ‘T_2+T_3’. Therefore, another phase boundary exists between the 0.85 and 0.90 compositions. The seventh phase boundary of the solid solution, although possibly ambiguous one, as more studies are needed for confirmation, is expected to lie in the composition range $0.975 \leq x \leq 1$, where two tetragonal phases merge into a single one.

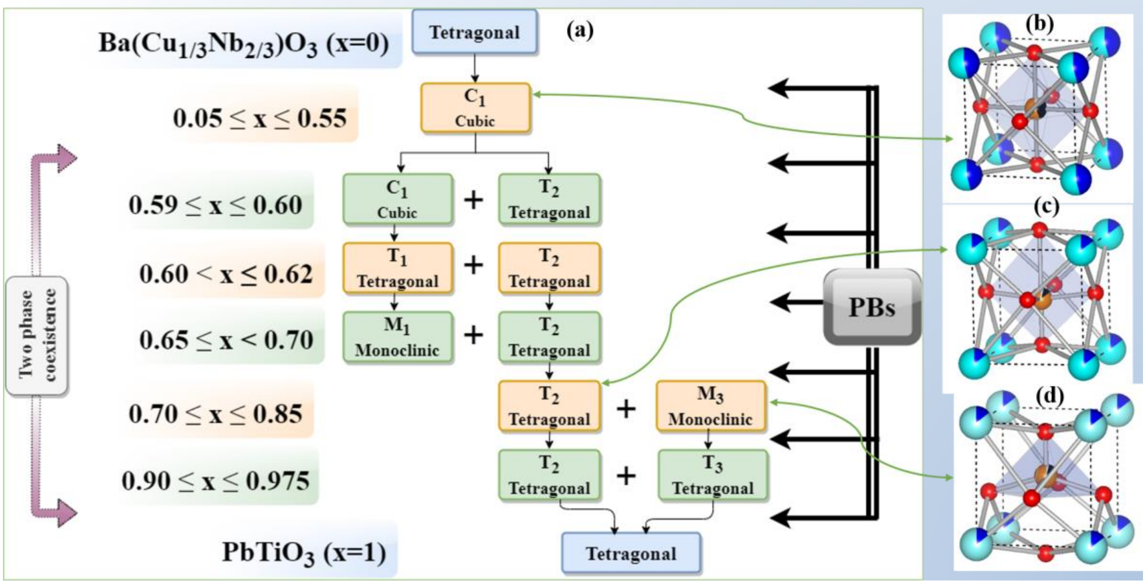

Fig 3.3 (a) A schematic presentation of phase progression in (1-x)BCN-(x)PT solid solution with the probable location of phase boundaries (PBs); 3D schematic weighted unit cells for (b) cubic, (c) tetragonal and (d) monoclinic. The red, sky blue, Prussian blue, colored sphere correspond to O, Pb, Ba, while body centre has Ti, Nb and Cu atoms in orange, black and white color, respectively

It's fascinating to observe how the crystal structural evolution occurs in this solid solution; as a result, phase 2 maintains its tetragonal lattice structure from the 0.59 to 0.90 composition in order to achieve a structure similar to that of the PT [see tetragonal tailing in Fig 3.1(c)]. A very careful and exhaustive Rietveld structure refinement has been carried out to unambiguously confirm the phase stabilities and structure for all these compositions. The following subsections (3.5.1 and 3.5.6) present detailed analysis of phase boundaries and crystal structure solutions for each composition considered above for an HR-XRD pattern.

The representation of graphics showing Rietveld fits of XRD patterns is the same for all the figures comprising Rietveld fits in this thesis. The red circles, black overlapping curves, and blue profiles represent the observed, calculated XRD patterns and the difference between them, respectively. The vertical green tick marks above the difference plot show the positions of the Bragg's peaks, and the corresponding crystal symmetry is written right next to them in a framed box.

3.5.1 Crystal Structure for the Composition Region 0.05 $\leq$x $\leq$ 0.55

At RT, the cubic crystal structure in the *Pm*-3*m* space group rapidly evolves after adding as little as 5 mol% PT content (x = 0.05) with BCN, and the cubic structure apparently remains stable up to the 0.55 composition. This is clearly evidenced from the XRD patterns shown in Fig 3.3(a), as all the x-ray diffraction profiles for these compositions are singlets, without any peak splitting. A Rietveld structure refinement has been carried out to confirm it further, considering the *Pm*-3*m* space group for these compositions (0.05 $\leq$x $\leq$ 0.55). A very good fit between observed and calculated XRD profiles is obtained with cubic structure, as can be seen from the fits shown in Fig 3.4, for three selected reflections (111), (200), and (220), of the 0.20, 0.40 and 0.55 compositions.

Both the 0.05 and 0.10 compositions exhibit cubic symmetry with a *Pm*-3*m* space group, similar to the 0.20 composition. For further comprehensiveness, the structure of the 0.55 composition was also analyzed by considering the two cubic phases 'C_1+C_2' (*Pm*-3*m* + *Pm*-3*m*) as well as coexisting cubic (*Pm*-3*m*) and tetragonal (*P*4*mm*) phases, i.e., 'C_1+T_2'. However, no notable improvement is obtained in the fits between the observed and Rietveld-calculated diffraction profiles. Since the structure of pure BCN is tetragonal, a narrow phase coexistence region of cubic and tetragonal phases and a phase boundary is expected in the composition range $0 < x < 0.05$. The precise location and attributes of this phase boundary and phase coexistence region can be discovered by investigating more compositions at close intervals.

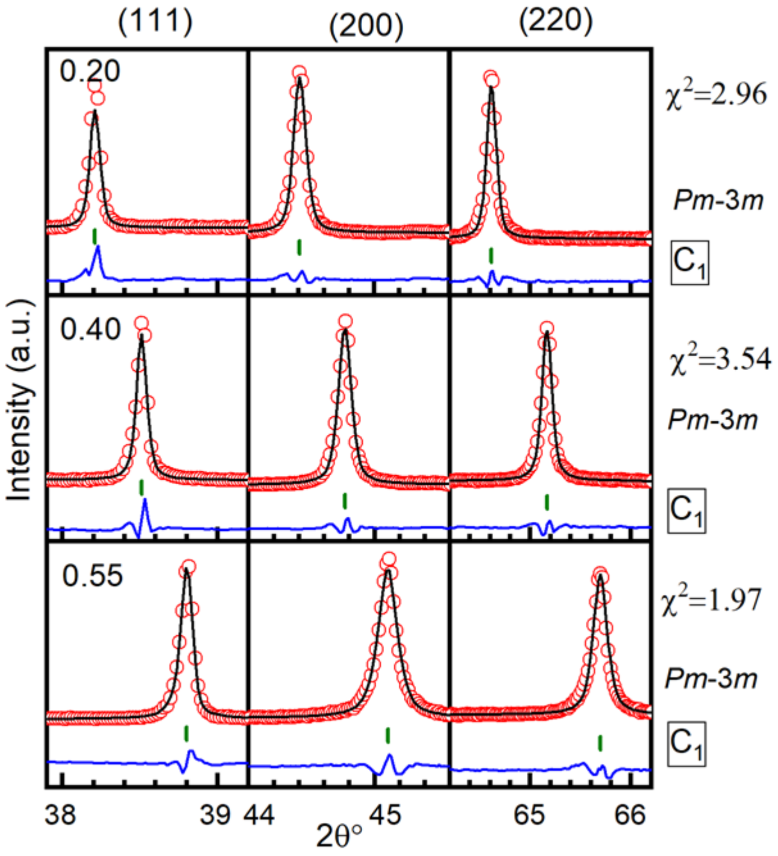

Fig 3.4 Rietveld fit of the cubic (111), (200) and (220) XRD peak profiles for x = 0.20, 0.40 and 0.55 compositions.

3.5.2 Crystal Structure for the Composition Region $0.59 \leq x \leq 0.60$

While refining the crystal structure of compositions higher PT content than the 0.55 composition, it is observed that every composition is, in fact, a combination of two crystallographic phases up to x = 0.975. As can be seen from Fig 3.5(a) and Fig 3.5(b), the (200) diffraction profiles for the composition range $0.59 \leq x \leq 0.60$ exhibit a triplet-like appearance. The diffraction pattern of these compositions can be well fitted by considering coexisting cubic (*Pm*-3*m*) and tetragonal (*P*4*mm*) phases (‘C_1+T_2’) as shown in Fig 3.5(a) for (111), (200) and (220) pseudocubic reflections. For completeness, the two-coexisting tetragonal (*P*4*mm*) phases (‘T_1+T_2’) with slightly different tetragonality to model the structure have also been considered in this composition range. A comparable χ^2 value have been obtained for both the phase coexistence. By adopting higher symmetry as best fit with a χ^2 value 1.92, the C+T combination is decided as the adequate structure for the x=0.60 composition. The structure confirms that, the composition 0.59 also possesses the coexisting ‘C_1+T_2’ crystal structure symmetry, similar to the 0.60 composition (see the Rietveld fit of Fig 3.5(b)).

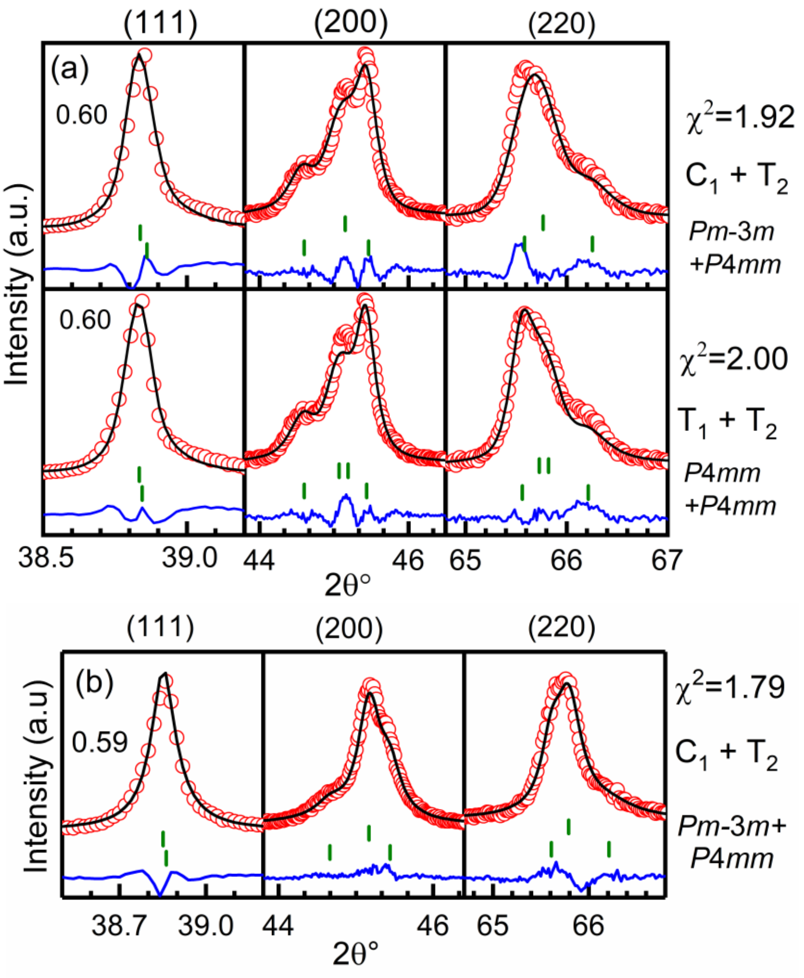

Fig 3.5 Rietveld Refinement fit for pseudocubic (111), (200) and (220) XRD peak profiles of (a) 0.60 composition using different structural models ‘T_1+T_2’ and ‘C_1+T_2’ for the illustration of competing crystal structures and (b) the 0.59 composition considering coexisting ‘C_1+T_2’ crystal structure

3.5.3 Crystal Structure for the Composition Region $0.60 < x \leq 0.62$

As shown in Fig 3.1(a) and Fig 3.6, the (200) and (220) XRD profiles for the x = 0.62 composition appear as doublets, while (111) has a singlet appearance. Such peak splitting characterizes the tetragonal structure in the *P*4*mm* space group. However, the Rietveld structure refinement reveals that a single-phase tetragonal structure in the *P*4*mm* space group gives a higher χ^2 (3.4) value and cannot fit the observed XRD pattern well, as shown in the lower panel of Fig 3.6. Therefore, various other plausible phase coexistence models containing the coexistence of monoclinic, tetragonal and cubic structures have been considered to refine the crystal structure of the 0.62 composition. A combination of cubic and tetragonal phases, 'C_1+T_2' (*Pm*-3*m* + *P*4*mm*), resulted in an inadequate fit with a higher χ^2 value of 3.2, as can be seen from Fig 3.6. The best fit was obtained by two coexisting tetragonal phases, 'T_1+T_2' (*P*4*mm*+ *P*4*mm*), with slightly different tetragonal distortion and lattice parameters. The low c/a tetragonal phase is adjusted between the broadening peak tails of the high c/a tetragonal phase. Some of the similar Pb-based systems like PZT and PMN-PT compositions close show similar behaviour near the MPB. For example in PMN-PT, the diffused tails of tetragonal structure was fitted with monoclinic phase [79] and in PZT, the tetragonal phase peaks is fitted in the diffused tails of the monoclinic peaks [80]. Consideration of a similar phase coexistence for (1-x)BCN-(x)PT in the composition range $0.60 < x \leq 0.62$ do not give the good Rietveld fit for the XRD pattern. Therefore, a 'T_1+T_2' phase combination is the most suitable crystal structure for the 0.62 composition possessing the lowest χ^2 value of 1.9.

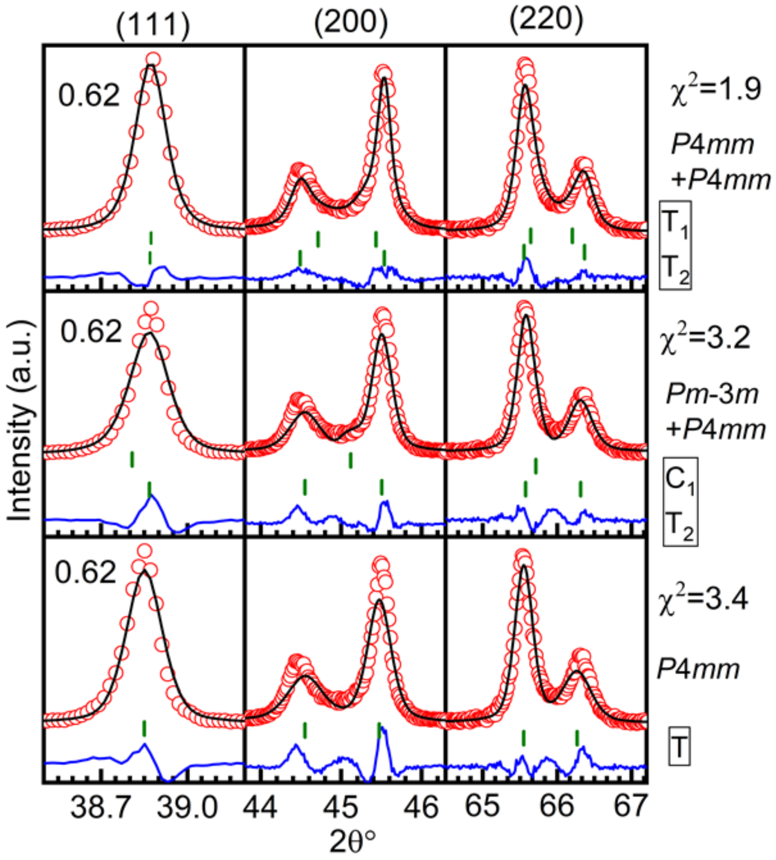

Fig 3.6 Rietveld fit for pseudocubic (111), (200) and (220) XRD peak profiles of the 0.62 composition using different phase combinations, namely, 'T_1+T_2', 'C_1+T_2' and 'T'

3.5.4 Crystal Structure for the Composition Region $0.62 < x \leq 0.65$

In contrast to the 0.62 composition, the XRD peaks for the 0.65 composition, exhibit asymmetry in all three pseudocubic (111), (200) and (220) profiles, as shown in Fig 3.1(a) and Fig 3.7. This infers a coexistence of monoclinic and tetragonal phases for these compositions as observed in many other MPB systems. The 0.65 composition is also fitted with two different combinations of the coexisting monoclinic (*Pm*) and tetragonal (*P*4*mm*) crystal structures, 'M_1+T_2' and 'T_2+M_3', as shown in Fig 3.7. Apart from the coexisting monoclinic and tetragonal structures, we also considered other plausible structure and their coexistence but none of them were able to account for the experimental XRD pattern in this composition range.

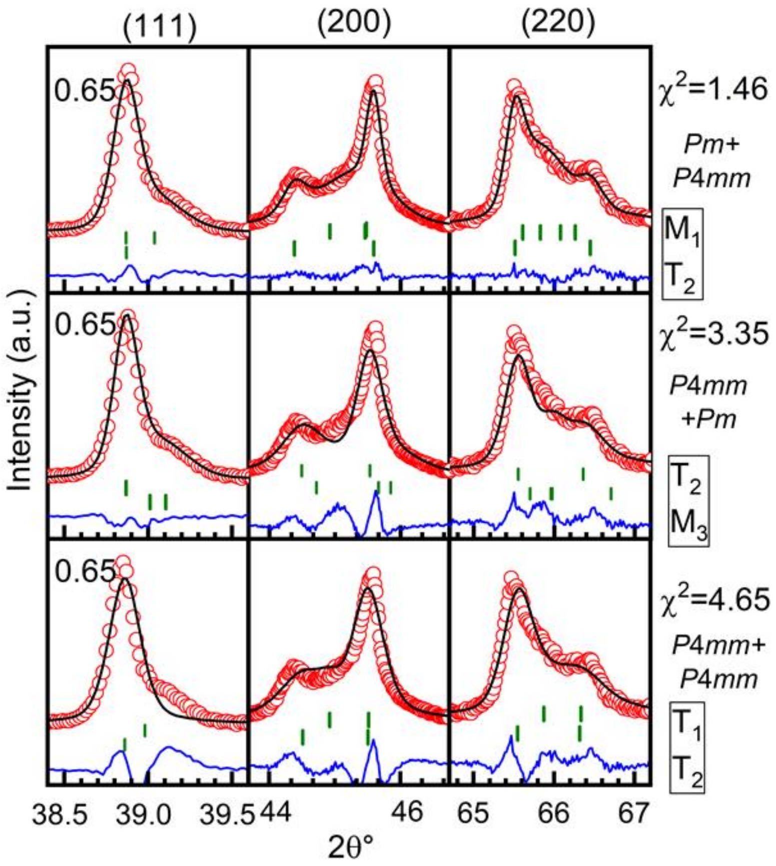

Fig 3.7 Rietveld fit for pseudocubic (111), (200) and (220) XRD peak profiles of the 0.65 composition using different coexisting crystal structures, namely, 'M_1+T_2', 'T_2+M_3' and 'T_1+T_2'

The first combination (upper panel in Fig 3.7) has phase 1 as monoclinic and phase 2 as tetragonal symmetry, i.e., 'M_1+T_2'. In it, the XRD peaks for monoclinic structure lie in between the (200) and (220) tetragonal doublet peaks, whereas in the second 'T_2+M_3' model (middle panel in Fig 3.7), it's the other way around due to the different consideration of the lattice parameters and unit cell volume values. For completeness, a coexistence of the two tetragonal 'T_1+T_2' structures, is also considered to fit the XRD pattern of 0.65 composition, but it turned out to be far off from the experimental data having a high χ^2 value of 4.65. The best fit is achieved for the 'M_1+T_2' phase coexistence model. The second model ('T_2+M_3') gives a poor fit for x =

0.65, but as shown in the next section, it (‘T_2+M_3’) is the best choice for the 0.70 composition. There is a significant difference in the goodness of fit and χ^2 values for both the monoclinic and tetragonal coexistence models for the 0.65 composition. The ‘M_1+T_2’ giving a much lower χ^2 (1.46) than the ‘T_2+M_3’ (3.35) combination. Thus one can make an unambiguous decision in favour of the ‘M_1+T_2’ phase coexistence model. All the compositions in the range $0.62 < x \leq 0.65$ can be well fitted considering the same structure as for 0.65 composition.

3.5.5 Crystal Structure for the Composition Region $0.70 \leq x \leq 0.85$

As discussed earlier, the nature of the diffraction profiles for the $0.70 \leq x \leq 0.85$ composition range is completely different from the 0.65 composition. It is observed that the monoclinic structure appearing in this composition range has a different set of lattice parameters than those observed in the $0.62 < x \leq 0.65$ composition range. Comparative Rietveld fits of the (111), (200) and (220) pseudocubic peak profiles for the composition 0.70 consisting of different crystal structure combinations are shown in Fig 3.8(a). The upper two panels of Fig 3.8(a) show coexisting tetragonal and monoclinic phases (Pm + P4mm) with different plausible sets of lattice parameters in the monoclinic structure similar to what we did in earlier section. The Rietveld fit for two coexisting tetragonal structures has also been shown in the lower panels of Fig 3.8(a). It can be deduced from these fits that an appropriate choice for the crystal structure solution of the 0.70 composition is indeed the coexistence of tetragonal and monoclinic phases (T_2+M_3) with lowest $\chi^2 = 2.3$ which is different from the composition range $0.62 < x \leq 0.65$. All the compositions in the range $0.70 \leq x \leq 0.85$ are verified to exhibit coexisting tetragonal and monoclinic structures, similar to 0.70 composition. For these compositions, however, the previous monoclinic phase (M_1) present in the composition range $0.62 < x \leq 0.65$ vanishes, and a new monoclinic phase with a comparatively much lower unit cell volume and different lattice parameters appears (M_3) that coexists with the tetragonal 'T_2' structure. This 'M_3' phase can be considered to arise from a PT-like lattice, as also illustrated in Fig 3.1(b). A very good fit between experimental and calculated XRD patterns is obtained for all the compositions in the range $0.70 \leq x \leq 0.85$, considering 'T_2+M_3' ($P4mm + Pm$) phase coexistence model, as illustrated in Fig 3.8(b). With increasing PT concentration from 0.70 to 0.85, the phase fraction of the monoclinic phase (M_3) continuously increases, as evidenced by the enhanced intensity of the higher 2θ angle XRD peak profile (appearing due to the monoclinic phase) in pseudocubic (111) XRD profile. It is easy to conclude that the fraction of the PT-like lattice monoclinic M_3 phase grows gradually from the 0.70 composition and becomes almost equal to the tetragonal phase (T_2) in the 0.85 composition. Moreover, the presence of the same monoclinic phase (M_3) in higher compositions (0.80 and 0.85) makes it clear that the best suitable phase combination for the 0.70 composition is indeed a coexistence of 'T_2+M_3'.

The appearance of two different kinds of monoclinic phases in the composition regions $0.62 < x \leq 0.65$ and $0.70 \leq x \leq 0.85$ is quite intriguing and raises some additional questions about the origin of these structures. A temperature-dependent structural analysis of various compositions in this range sheds light on such phase coexistence and is described in the next chapter.

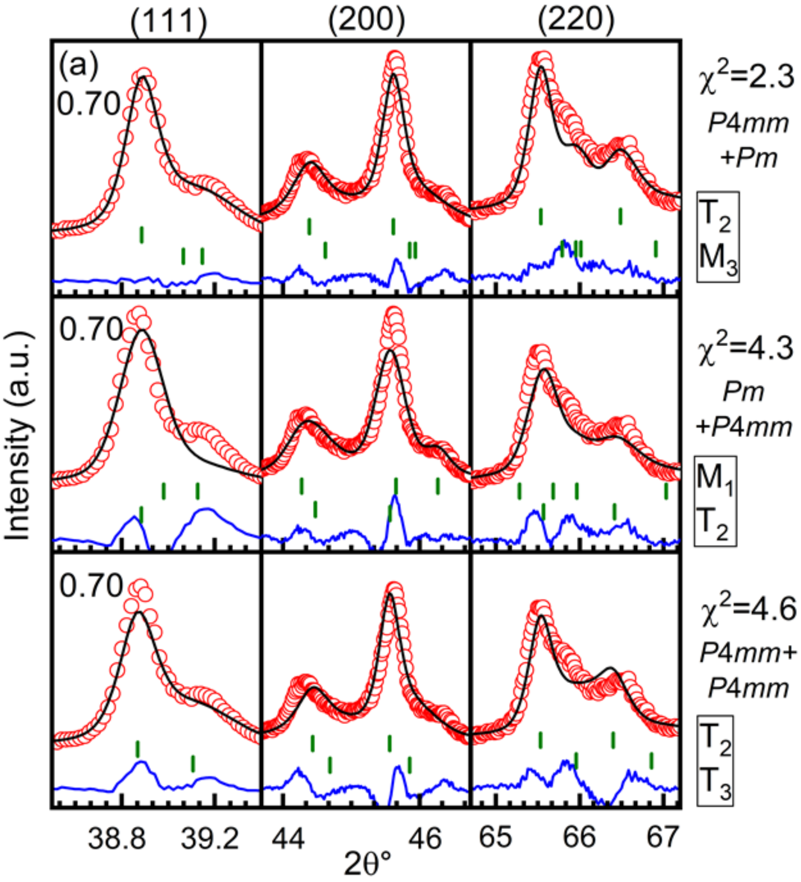

Fig 3.8 Rietveld fit for pseudo cubic (111), (200) and (220) XRD peak profiles of (a) the 0.70 composition using different plausible coexisting crystal structures, namely, ‘T_2+M_3’, ‘M_1+T_2’, and ‘T_1+T_2’

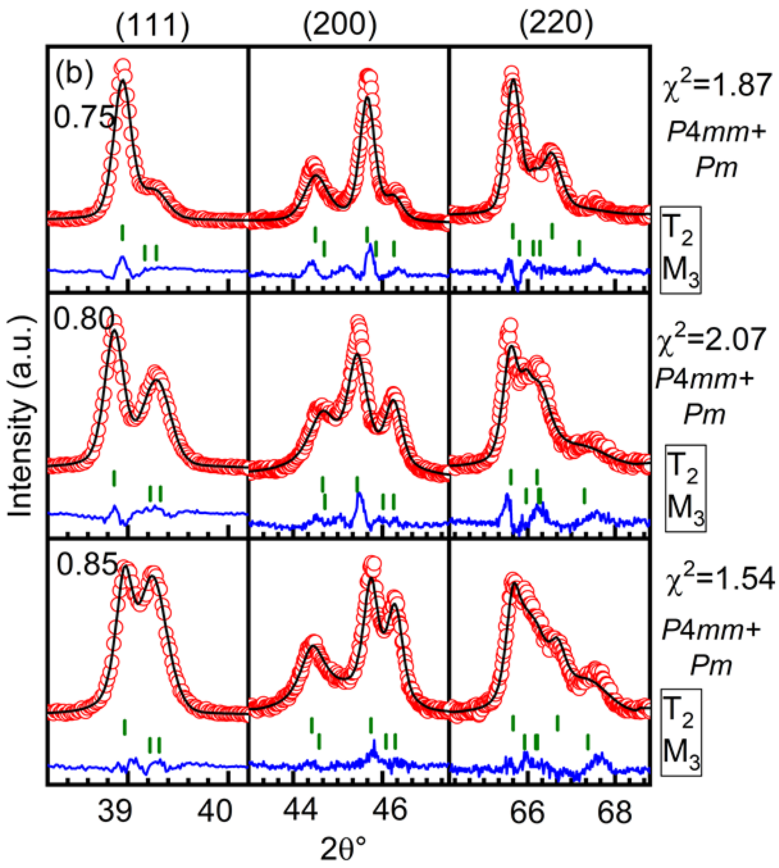

Fig 3.8 Rietveld fit for pseudo cubic (111), (200) and (220) XRD peak profiles of (b) various compositions in the range $0.70 \le x \le 0.85$ considering coexisting 'T_2+M_3' structures

3.5.6 Crystal Structure for the Composition Region 0.85 < x < 1

The nature of the diffraction profiles changes again for the compositions in the range $0.85 < x < 1$. A first look at the diffraction profiles suggests that the structure of these compositions is closer to the tetragonal structure in the *P*4*mm* space group as reported for pure PT. The pseudocubic (111) XRD profile appears almost as a singlet, while (220) appears as a doublet. The pseudocubic (200) is also a clear doublet for the 0.95 and 0.975 compositions, but in the 0.90 composition, there is a clear additional asymmetry in the peak of the (002)/(200) doublet. This suggests that there is an additional coexisting crystal structure in this composition. To solve the crystal structure of the 0.90 composition, various plausible competitive crystal structure combinations, ‘T_2+T_3’ (*P*4*mm* + *P*4*mm*), ‘T_2+M_3’ (*P*4*mm*+*Pm*) and ‘T_2+C_3’ (*P*4*mm*+*Pm*-3*m*), have been considered to fit the experimental XRD pattern in the Rietveld Refinement, as depicted in Fig 3.9(a). The calculated XRD patterns for the ‘T_2+C_3’ combinations are too far to fit the experimental pattern adequately. The phase coexistence ‘T_2+M_3’ on the other hand is quite comparable to the combination ‘T_2+T_3’ and no significant improvement has been observed in the fit. Therefore, the highest symmetry combination of structure of the two coexisting tetragonal structures, ‘T_2+T_3’ (*P*4*mm* + *P*4*mm*), is considered as the valid structural combination for this composition. The XRD patterns of the 0.90 and 0.95 compositions look somewhat different from one another but share the same crystal symmetry. Such a state is caused by the difference in the phase fraction and tetragonality of the two coexisting tetragonal phases, as evidenced by the Rietveld Refinement. The 0.95 and 0.975 compositions appear to be similar to a single-phase tetragonal structure, so their comparative fits have also been done using single-phase and two-phase models. Both the compositions have a tetragonal structure with *P*4*mm* space group, as shown in Fig 3.9(b) and Fig 3.9(c) illustrating the (200), (210) and (220) pseudocubic reflections. For both these compositions, a slightly better fit and lower χ^2 values are obtained for the two-phase coexistence model. In these compositions, both the tetragonal structure appears to originate from PT-like lattices. The XRD patterns for the 0.95 and 0.975 compositions are also well fitted by considering two coexisting tetragonal structures, ‘T_2+T_3’, as shown in 3.9(b) and Fig 3.9(c), and all the final crystal structure solutions are illustrated collectively in 3.9(d). With increasing composition from 0.90 to 0.975, the fraction of the second coexisting tetragonal phase gradually decreases and soaks into the higher tetragonality phase, eventually disappearing for pure PT.

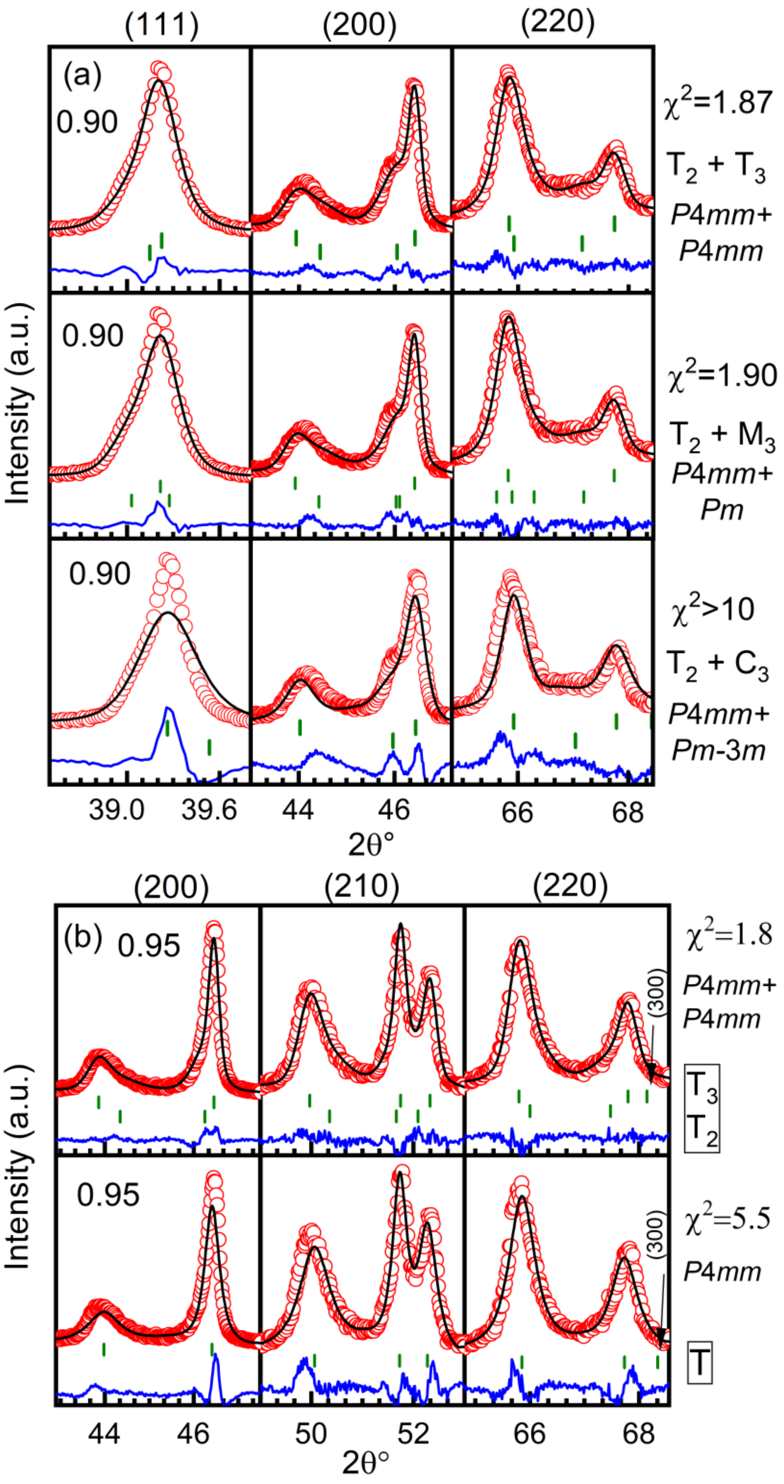

Fig 3.9 Rietveld fit for pseudo cubic (111), (200) and (220) XRD peak profiles using various plausible structural models of (a) the 0.90 composition for ‘T_2+T_3’, ‘T_2+M_3’, and ‘T_2+C_3’; (b) 0.95 composition for ‘T_2+T_3’ and ‘T’

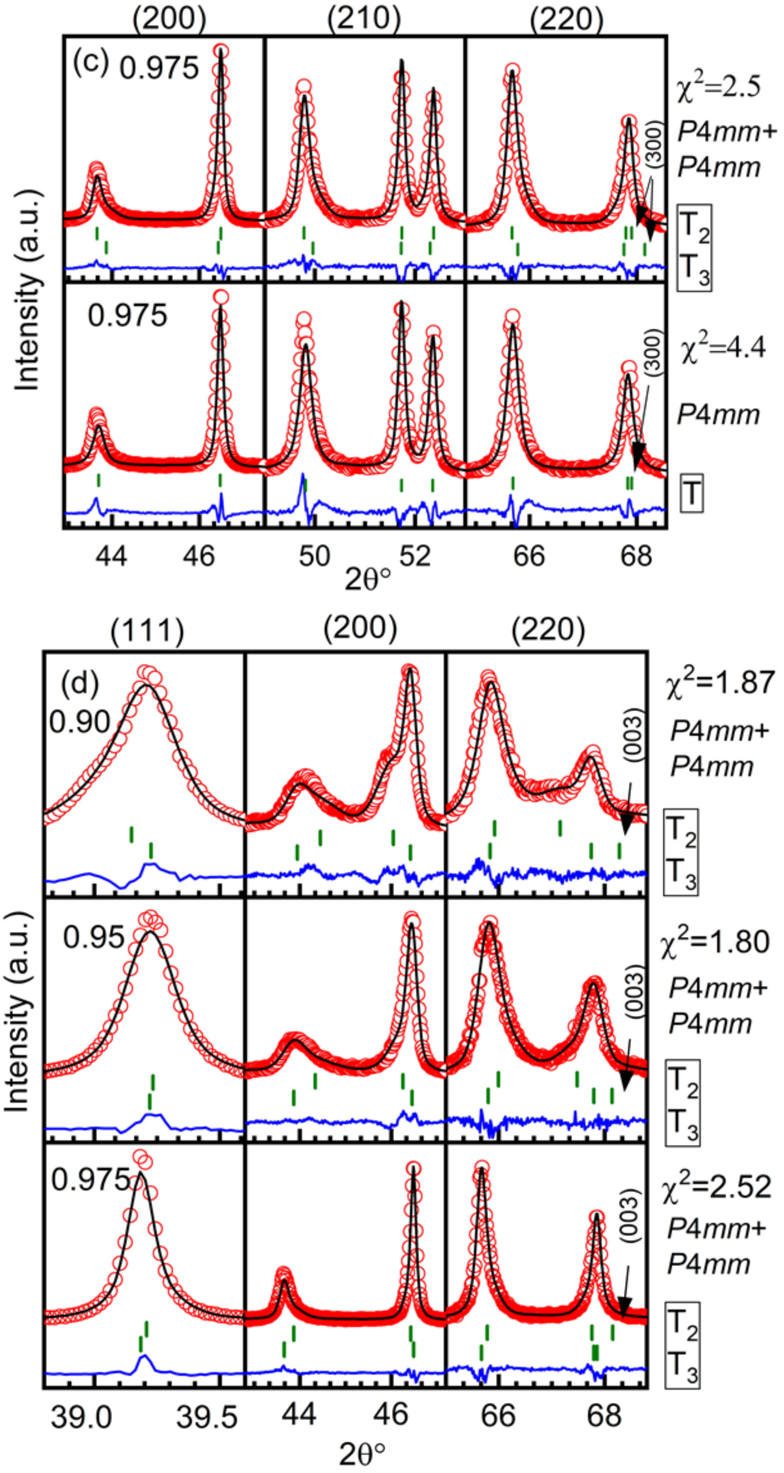

Fig 3.9 Rietveld fit for different pseudo cubic XRD peak profiles using various plausible structural models of (c) 0.975 composition for ‘T_2+T_3’ and ‘T’; (d) final Rietveld fits for two coexisting tetragonal structures for the compositions in $0.90 \leq x \leq 0.975$ range

3.6 Rietveld Refined Structural Parameters and Fit for the Entire Composition Range of (1-x)BCN-(x)PT

Full pattern Rietveld refinement fits for HR-XRD data [λ = 1.5406 ($CuK_{\alpha1}$)] (2θ range: 20° to 110°) of some representative compositions are given in Fig 3.10(a) x = 0, 0.20, 0.40 and 0.55; (b) 0.59, 0.60, 0.62 and 0.65; (c) 0.70, 0.75, 0.80 and 0.85 and (d) 0.90, 0.95 and 0.975 considering the respective structural solutions discussed in earlier sections. The Tables containing the refined structural parameters of the composition x = 0 (BCN) for tetragonal structure, 0.55 for cubic structure, 0.60 for a coexisting cubic and tetragonal structures, 0.62, 0.90, 0.95 and 0.975 for two coexisting tetragonal structures, and 0.65, 0.70, 0.80, and 0.85 for the coexisting tetragonal and monoclinic structures are given in Table 3.1 to Table 3.13.

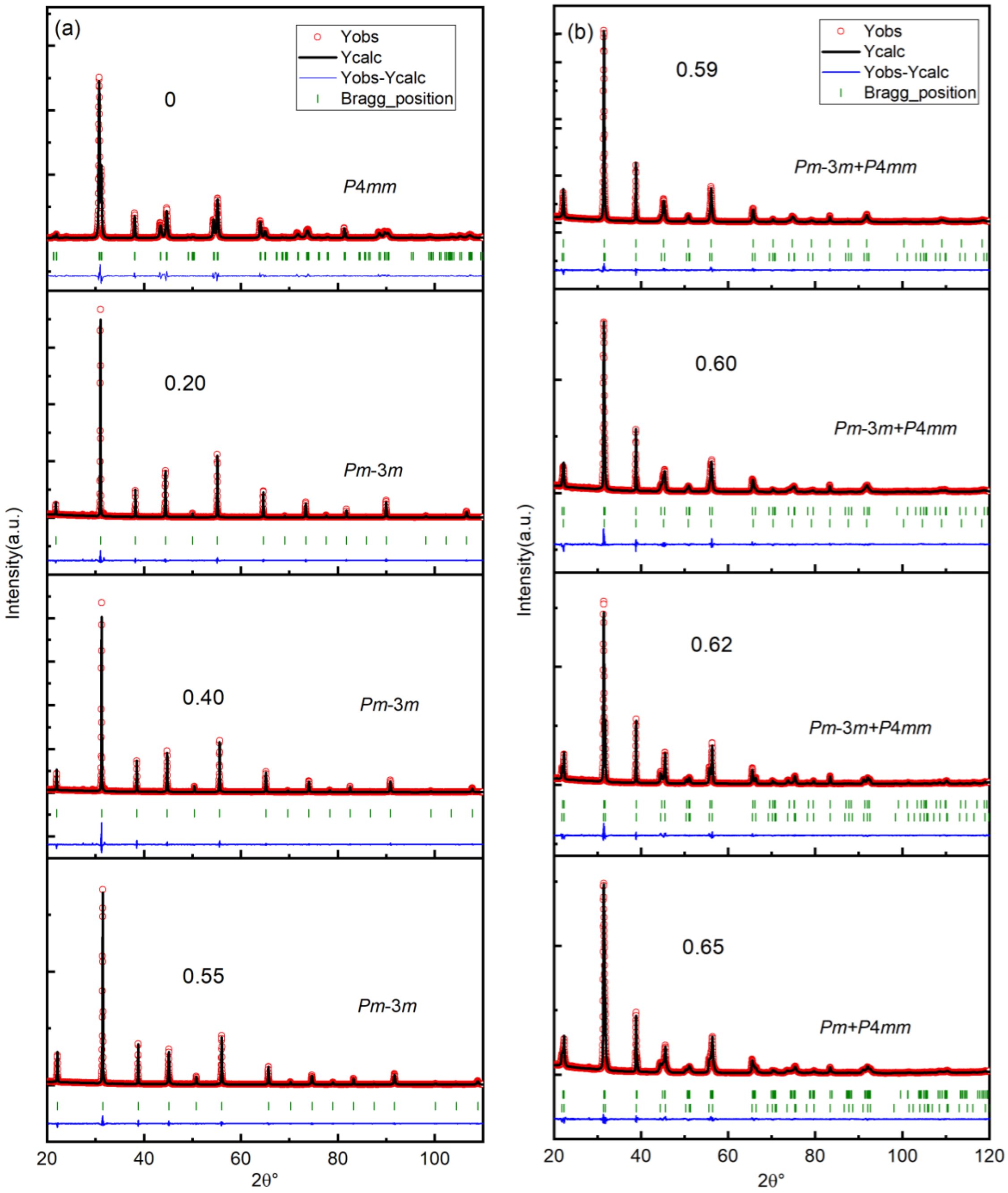

Fig 3.10 Full pattern Rietveld Refinement fits of HR-XRD patterns for x = (a) 0, 0.20, 0.40 and 0.55; (b) 0.59, 0.60, 0.62 and 0.65 compositions

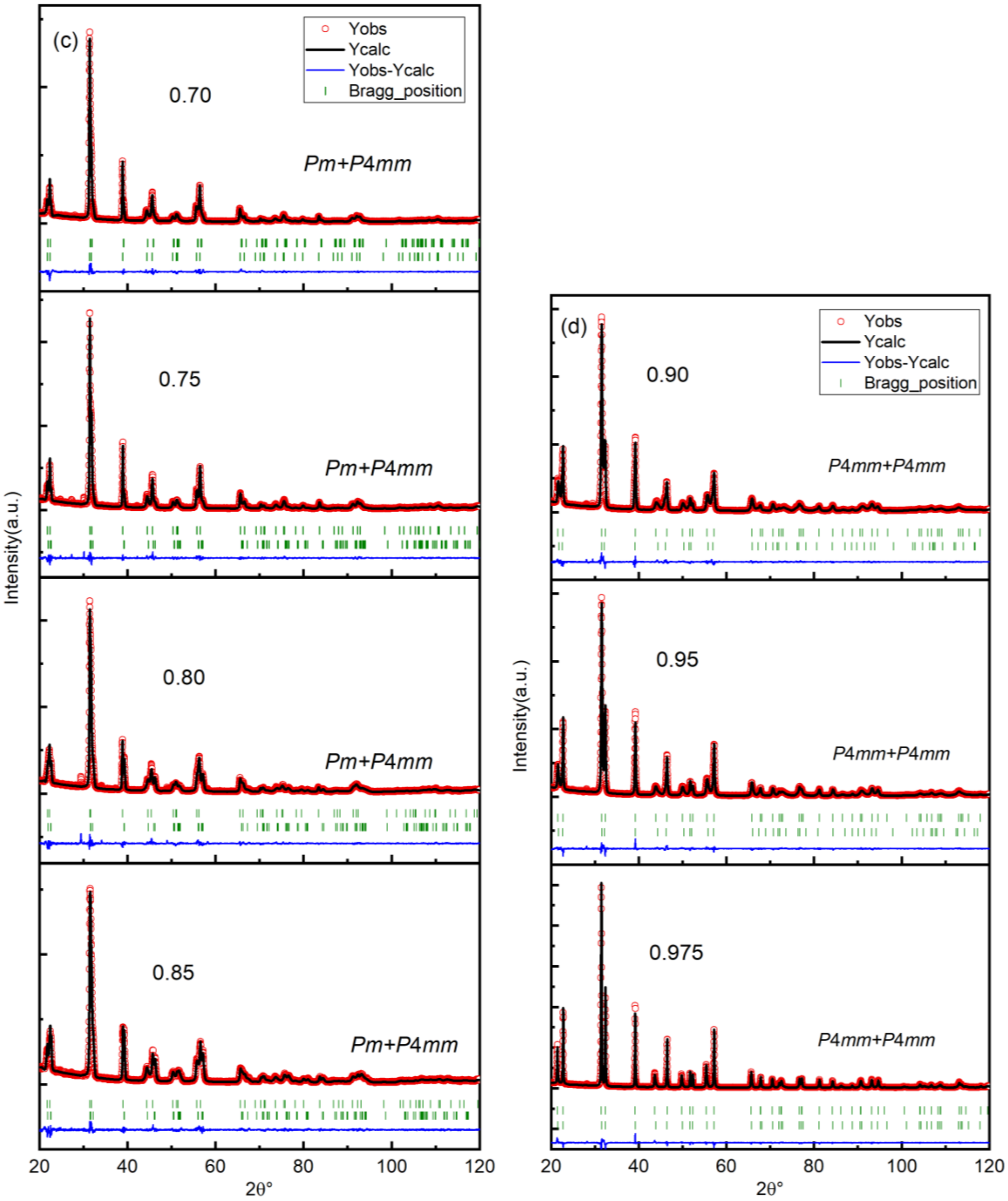

Fig 3.10 Full pattern Rietveld Refinement fits of HR-XRD patterns for x = (c) 0.70, 0.75, 0.80 and 0.85; (d) 0.90, 0.95 and 0.975 compositions

Table 3.1 Refined crystal structural parameters for composition x = 0

Crystal System		BCN (Tetragonal)			
Lattice Parameter (A)	a; c; c/a	4.0578(1); 4.1713(1) 1.0279			
Unit Cell Vol.(A^3)		68.686(4)			
Phase fraction (%)		100			
Position Coordinates		x	y	z	B
$X_{(Ba/Pb)}$		0.0	0.0	0.0	1.35(9)
$X_{(Cu/Nb/Ti)}$		0.5	0.5	0.502(6)	0.86(13)
X_{O1}		0.5	0.5	0.048(6)	2.30(19)
X_{O2}		0.5	0.0	0.521(7)	1.63(4)
R_{wp}		11.9			
R_{exp}		6.43			
R_p		9.05			
χ^2		3.42			

Table 3.2 Refined crystal structural parameters for composition x = 0.20

Crystal System for 0.20		Cubic (C_1)			
Lattice Parameter (Å)	a	4.0763(1)			
Unit Cell Vol. (Å^3)		67.733(6)			
Phase fraction (%)		100			
Position Coordinates		x	y	z	B
$X_{(Ba/Pb)}$		0.0	0.0	0.0	1.25(3)
$X_{(Cu/Nb/Ti)}$		0.5	0.5	0.5	0.72(2)
X_O		0.5	0.5	0	0.59(9)
R_{wp}		10.9			
R_{exp}		6.32			
R_p		7.52			
χ^2		2.96			

Table 3.3 Refined crystal structural parameters for composition x = 0.40

Crystal System for 0.40		Cubic (C_1)			
Lattice Parameter (Å)	a	4.0456(1)			
Unit Cell Vol. (Å^3)		66.214(8)			
Phase fraction (%)		100			
Position Coordinates		x	y	z	B
$X_{(Ba/Pb)}$		0.0	0.0	0.0	1.49(4)
$X_{(Cu/Nb/Ti)}$		0.5	0.5	0.5	0.72(2)
X_O		0.5	0.5	0	0.35(6)
R_{wp}		10.9			
R_{exp}		5.75			
R_p		8.10			
χ^2		3.54			

Table 3.4 Refined crystal structural parameters for composition x = 0.55

Crystal System for 0.55		Cubic (C_1)			
Lattice Parameter (Å)	a	4.0167(2)			
Unit Cell Vol. (Å^3)		65.800(9)			
Phase fraction (%)		100			
Position Coordinates		x	y	z	B
$X_{(Ba/Pb)}$		0.0	0.0	0.0	2.1(9)
$X_{(Cu/Nb/Ti)}$		0.5	0.5	0.5	0.4(9)
X_O		0.5	0.5	0	1.3(9)
R_{wp}		8.04			
R_{exp}		5.72			
R_p		6.14			
χ^2		1.97			

Table 3.5 Refined crystal structural parameters for composition x = 0.60

Crystal System for 0.60		Cubic (C_1)				Tetragonal (T_2)			
Lattice Parameter (Å)	a; c	4.0144(1)				3.9882(1); 4.0632(2)			
Unit Cell Vol. (Å^3)		64.696(2)				64.630(4)			
Phase fraction (%)		48.88(0.68)				51.12(0.64)			
Position Coordinates		x	y	z	B	x	y	z	B
$X_{(Ba/Pb)}$		0.0	0.0	0.0	2.13(5)	0.0	0.0	0.0	0.54(2)
$X_{(Cu/Nb/Ti)}$		0.5	0.5	0.5	0.19(9)	0.5	0.5	0.501(3)	0.31(5)
X_{O1}		0.5	0.5	0	0.7(2)	0.5	0.5	0.075(5)	0.8(5)
X_{O2}		-	-	-	-	0.5	0.0	0.530(5)	0.5(3)
R_{wp}		8.00							
R_{exp}		5.74							
R_p		6.09							
χ^2		1.94							

Table 3.6 Refined crystal structural parameters for composition x = 0.62

Crystal System for 0.62		Tetragonal (T_1)				Tetragonal (T_2)			
Lattice Parameter (Å)	a; c	3.9894(1); 4.0502(3)				3.9807(1); 4.0694(1)			
Unit Cell Vol. (Å^3)		64.461(7)				64.486(3)			
Phase fraction (%)		52.82(0.74)				45.18(0.72)			
Position Coordinates		x	y	z	B	x	y	z	B
$X_{(Ba/Pb)}$		0.0	0.0	0.0	1.46(3)	0.0	0.0	0.0	1.13(3)
$X_{(Cu/Nb/Ti)}$		0.5	0.5	0.510(2)	0.33(4)	0.5	0.5	0.511(3)	0.17(5)
X_{O1}		0.5	0.5	0.039(8)	0.04(4)	0.5	0.5	0.084(4)	1.55(4)
X_{O2}		0.5	0.0	0.542(8)	3.4(3)	0.5	0.0	0.536(5)	0.25(1)
R_{wp}		8.37							
R_{exp}		5.98							
R_p		6.64							
χ^2		1.89							

Table 3.7 Refined crystal structural parameters for composition x = 0.65

Crystal System	Monoclinic (M_1)				Tetragonal (T_2)			
Lattice Parameter (Å) a; c	3.9854(4); 3.987(4); 4.0325(3); β = 90.362(4)				3.9762(1); 4.0793(2)			
Unit Cell Vol. (Å^3)	64.073(9)				64.497(4)			
Phase fraction (%)	67.45(0.60)				33.55(0.57)			
Position Coordinates	x	y	z	B	x	y	z	B
$X_{(Ba/Pb)}$	0.0	0.0	0.0	1.67(2)	0.0	0.0	0.0	1.30(3)
$X_{(Cu/Nb/Ti)}$	0.544(2)	0.5	0.522(2)	0.03(5)	0.5	0.5	0.517(2)	0.08(2)
X_{O1}	0.49(14)	0.5	0.012(9)	0.38(4)	0.5	0.5	0.079(4)	0.81(5)
X_{O2}	0.51(14)	0.0	0.450(5)	0.52(1)	0.5	0.0	0.504(6)	0.42(7)
X_{O3}	0.153(3)	0.5	0.468(8)	1.8(5)	-	-	-	-
R_{wp}	6.28							
R_{exp}	5.20							
R_p	4.72							
χ^2	1.46							

Table 3.8 Refined crystal structural parameters for composition x = 0.70

Crystal System	Tetragonal (T_2)				Monoclinic (M_3)			
Lattice Parameter (Å) a; c	3.9848(1); 4.0688(2)				3.9278(4); 3.9206(5); 4.0827(2); β = 90.568(2)			
Unit Cell Vol. (Å^3)	64.610(13)				63.45(10)			
Phase fraction (%)	92.78(0.85)				6.8(0.04)			
Position Coordinates	x	y	z	B	x	y	z	B
$X_{(Ba/Pb)}$	0.0	0.0	0.0	1.15(2)	0.0	0.0	0.0	2.21(6)
$X_{(Cu/Nb/Ti)}$	0.5	0.5	0.502(3)	0.04(8)	0.525(2)	0.5	0.506(3)	0.70(4)
X_{O1}	0.5	0.5	0.085(3)	0.82(3)	0.538(3)	0.0	0.453(6)	1.11(8)
X_{O2}	0.5	0.0	0.532(5)	0.98(4)	0.100(6)	0.5	0.461(2)	1.18(8)
X_{O3}	-	-	-	-	0.610(7)	0.5	-0.061(4)	0.93(9)
R_{wp}	14.4							
R_{exp}	9.37							
R_p	11.0							
χ^2	2.34							

Table 3.9 Refined crystal structural parameters for composition x = 0.80

Crystal System for 0.80	Tetragonal (T_2)				Monoclinic (M_3)			
Lattice Parameter (Å) a; c	3.9886(1); 4.0549(2)				3.9358(4); 3.9223(2); 4.0502(4); β = 90.233(5)			
Unit Cell Vol. ($Å^3$)	64.514(4)				62.622(11)			
Phase fraction (%)	53.82(0.26)				46.18(0.23)			
Position Coordinates	x	y	z	B	x	y	z	B
$X_{(Ba/Pb)}$	0.0	0.0	0.0	1.15(2)	0.0	0.0	0.0	0.79(4)
$X_{(Cu/Nb/Ti)}$	0.5	0.5	0.527(4)	0.04(8)	0.555(3)	0.5	0.509(5)	0.76(8)
X_{O1}	0.5	0.5	0.096(3)	0.82(3)	0.553(8)	0.5	0.418(6)	0.68(7)
X_{O2}	0.5	0.0	0.523(2)	0.98(4)	0.084(3)	0.5	0.425(3)	0.81(7)
X_{O3}	-	-	-	-	0.566(5)	0.5	-0.095(6)	2.21(3)
R_{wp}	7.51							
R_{exp}	5.22							
R_p	5.60							
χ^2	2.07							

Table 3.10 Refined crystal structural parameters for composition x = 0.85

Crystal System for 0.85		Tetragonal (T_2)				Monoclinic (M_3)			
Lattice Parameter (Å)	a; c	3.9639(1); 4.0748(2)				3.9362(4); 3.9195(2); 4.0611(3); β = 90.193(9)			
Unit Cell Vol. (Å^3)		64.034(5)				62.655(9)			
Phase fraction (%)		50.07(0.38)				49.93(0.43)			
Position Coordinates		x	y	z	B	x	y	z	B
$X_{(Ba/Pb)}$		0.0	0.0	0.0	1.15(2)	0.0	0.0	0.0	0.51(3)
$X_{(Cu/Nb/Ti)}$		0.5	0.5	0.499(7)	0.04(8)	0.527(2)	0.5	0.514(3)	0.11(2)
X_{O1}		0.5	0.5	0.101(3)	0.82(3)	0.51(13)	0.0	0.420(8)	1.21(2)
X_{O2}		0.5	0.0	0.558(3)	0.98(4)	0.072(6)	0.5	0.36(2)	1.41(2)
X_{O3}		-	-	-	-	0.52(3)	0.5	-0.109(6)	3.43(9)
R_{wp}		7.04							
R_{exp}		5.70							
R_p		5.33							
χ^2		1.54							

Table 3.11 Refined crystal structural parameters for composition x = 0.90

Crystal System for 0.90		Tetragonal (T_2)				Tetragonal (T_3)			
Lattice Parameter (Å)	a;c	3.9089(1); 4.1190(2)				3.9355(2); 4.0786(4)			
Unit Cell Vol. (Å^3)		62.940(4)				63.172 (7)			
Phase fraction (%)		28.36(0.17)				71.64(0.29)			
Position Coordinates		x	y	z	B	x	y	z	B
$X_{(Ba/Pb)}$		0.0	0.0	0.0	0.10(3)	0.0	0.0	0.0	0.68(3)
$X_{(Cu/Nb/Ti)}$		0.5	0.5	0.531(2)	0.03(4)	0.5	0.5	0.494(4)	0.55(5)
X_{O1}		0.5	0.5	-0.100(5)	1.18(4)	0.5	0.5	-0.122(3)	0.85(8)
X_{O2}		0.5	0.0	0.587(3)	1.61(3)	0.5	0.0	0.578(3)	1.02(5)
R_{wp}		6.67							
R_{exp}		4.92							
R_p		5.07							
χ^2		1.83							

Table 3.12 Refined crystal structural parameters for composition x = 0.95

Crystal System		0.95 (Tetragonal +Tetragonal)							
Lattice Parameter(Å)	a; c	3.9227(1); 4.0821(3)				3.9062(1); 4.1247(1)			
Unit Cell Vol.(A^3)		62.810(2)				62.939(3)			
Phase fraction (%)		50.53(0.27)				49.47(0.12)			
Position Coordinates		x	y	z	B	x	y	z	B
$X_{(Ba/Pb)}$		0.0	0.0	0.0	1.33(3)	0.0	0.0	0.0	0.68(3)
$X_{(Cu/Nb/Ti)}$		0.5	0.5	0.531(2)	0.73(4)	0.5	0.5	0.533(2)	0.55(5)
X_{O1}		0.5	0.5	0.095(5)	0.75(4)	0.5	0.5	0.109(3)	0
X_{O2}		0.5	0.0	0.586(4)	1.61(3)	0.5	0.0	0.591(2)	0
R_{wp}		6.78							
R_{exp}		5.11							
R_p		5.21							
χ^2		1.80							

Table 3.13 Refined crystal structural parameters for composition x = 0.975

Crystal System		0.975 (Tetragonal +Tetragonal)							
Lattice Parameter(Å)	a; c	3.9034(1); 4.1434(1)				3.9082(1); 4.1244(4)			
Unit Cell Vol.(A^3)		63.133(10)				62.999(7)			
Phase fraction (%)		62.30(0.20)				37.70(0.35)			
Position Coordinates		x	y	z	B	x	y	z	B
$X_{(Ba/Pb)}$		0.0	0.0	0.0	1.33(3)	0.0	0.0	0.0	0.95(8)
$X_{(Cu/Nb/Ti)}$		0.5	0.5	0.546(2)	0.73(4)	0.5	0.5	0.535(3)	0.07(5)
X_{O1}		0.5	0.5	0.077(4)	0.75(4)	0.5	0.5	0.93(7)	1.04(3)
X_{O2}		0.5	0.0	0.600(3)	1.61(3)	0.5	0.0	0.620(4)	1.56(4)
R_{wp}		8.07							
R_{exp}		5.12							
R_p		6.31							
χ^2		2.52							

3.7 Composition-Dependent Variation of Lattice Parameters and Phase Boundaries for (1-x)BCN-(x)PT

Fig 3.11(a) depicts the composition-dependent variation of lattice parameters in the composition range $0.55 \leq x \leq 0.975$. The inset of this figure includes the same information for the remaining composition range, i.e., $0 \leq x < 0.55$. Based on the structural analysis results for various composition ranges presented in the preceding sections, the location of different structural phase boundaries is indicated by the vertical lines in Fig 3.11. The locations of these phase boundaries are anticipated on the basis of varying phase fractions, and their preciseness should not be given much attention. The value of the lattice parameters monotonously decreases with increasing PT concentration for the cubic structured compositions in the range of 0.20 to 0.55. For the compositions with $x > 0.55$, the lattice parameters exhibit an overall increasing trend for the ‘c’ parameters and a decreasing one for the ‘a’ parameters as the composition increases in PT content in almost all the appearing crystallographic phases, ultimately matching the high tetragonality (1.06) of PT [81]. However, due to high monoclinic distortions, exceptions exist around the 0.65 and 0.80 compositions in the form of small fluctuations in the determined lattice parameters for the phase boundary compositions where the phase fraction is an extremum. This can be either due to crystal structure instability at the phase boundary or some inaccuracy in the phase fraction determination of the minor coexisting phase, which is unavoidable. The composition-dependent phase fraction variation of the two coexisting phases in various composition ranges is shown in Fig 3.11(b).

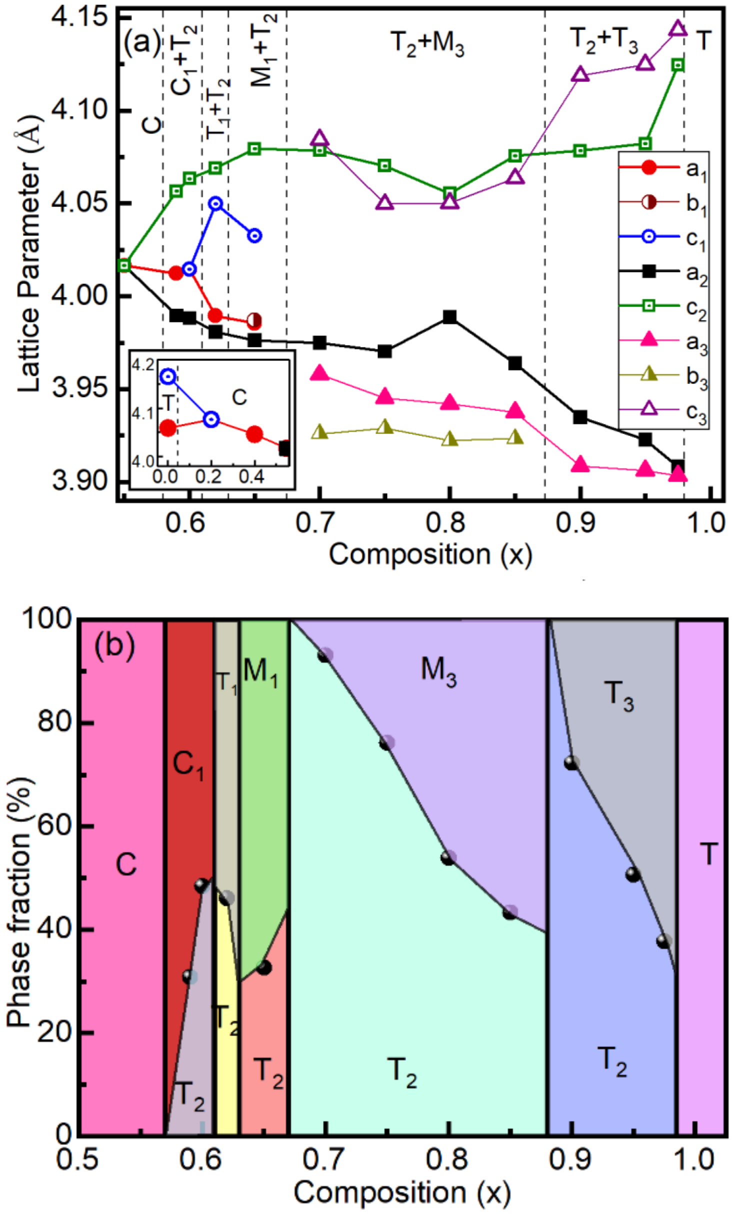

Fig 3.11 (a) Composition-dependent variation of unit cell lattice parameters in the range of $0.55 \leq x < 1$ for (1-x)BCN-(x)PT ceramics; The inset shows the same information for the composition range $0 \leq x \leq 0.55$; (b) Composition-dependent variation of crystallographic phase fractions in the composition range of $0.50 \leq x \leq 1$. The vertical lines in both figures represent the location of phase boundaries

Generally, in the solid solution of monophasic materials, the phase fraction varies from 0 to 100% when one phase gets converted into another within the span of an MPB [22,82]. However, an approximation effort has been made in Fig 3.11(b), where multiple phase boundaries are present. The crystal structure combination of the 0.59 and 0.60 compositions is almost same (‘C_1+T_2’), but a considerable increase in the phase fraction of the tetragonal phase (T_2) from approximately 30% to 50% is observed in this relatively tiny composition gap. The monoclinic phase (M_3) originates from the 0.70 composition and grows continuously with increasing PT content until it becomes almost equivalent to the tetragonal phase (T_2) for the 0.85 composition. After the next phase boundary, the phase fraction of phase 3 keeps going up from 0.90 to 0.975 composition. The number of compositions taken under this study is not sufficient to provide the exact trend of phase fraction variation throughout the complete composition range, especially in the region with phase combinations ‘T_1+T_2’ and ‘M_1+T_2’. All the refined structural parameters (unit cell parameter, unit cell volume and phase fractions) are listed in Table 3.14, Table 3.15 and Table 3.16, corresponding to phase 1, 2 and 3, respectively.

Table 3.14 Refined lattice parameters, unit cell volume and phase fraction of phase 1 in the composition range $0 \leq x \leq 0.65$ of (1-x)BCN-(x)PT solid solution

Phase 1 Composition -x		Lattice Parameters		Unit cell Volume (Å^3)	Phase fraction (%)
	a(Å)	b(Å); β(°)	c(Å)		
0	4.0578	-	4.1713	68.686	100
0.20	4.0763	-	-	67.733	100
0.40	4.0456	-	-	66.214	100
0.55	4.0167	-	-	64.800	100
0.59	4.0125	-	-	64.581	69.22
0.60	4.0144	-	-	64.696	48.88
0.62	3.9894	-	4.0502	64.461	53.82
0.65	3.9854	3.9872; 90.362	4.0325	64.073	67.45

Table 3.15 Refined lattice parameters, unit cell volume and phase fraction of phase 2 in the composition range 0.59 ≤ x ≤ 0.975 of (1-x)BCN-(x)PT solid solution

Phase 2 Composition (x)	Lattice Parameters		Unit cell Volume (Å ^{3})	Phase fraction (%)
	a(Å)	c(Å)		
0.59	3.9894	4.0567	64.563	30.73
0.60	3.9882	4.0632	64.630	51.12
0.62	3.9807	4.0694	64.486	45.18
0.65	3.9762	4.0793	64.497	32.55
0.70	3.9848	4.0688	64.610	92.78
0.75	3.9703	4.0702	64.161	76.16
0.80	3.9886	4.0549	64.514	53.82
0.85	3.9639	4.07948	64.034	50.07
0.90	3.9355	4.0786	63.172	71.64
0.95	3.9227	4.0821	62.810	50.53
0.975	3.9082	4.1244	62.999	37.70

Table 3.16 Refined parameters of phase 3 for the composition range 0.70 ≤ x ≤ 0.975 of (1-x)BCN-(x)PT solid solution

Phase 3 Composition (x)	Lattice Parameters			Unit cell Volume (Å^3)	Phase fraction (%)
	a(Å)	b(Å);β(°)	c(Å)		
0.70	3.9278	3.9206; 90.568	4.0827	63.45	6.8
0.75	3.9529	3.9235; 90.159	4.0495	63.31	23.85
0.80	3.9358	3.9223; 90.233	4.0502	62.622	46.18
0.85	3.9362	3.9195; 90.193	4.0611	62.655	49.93
0.90	3.9089	-	4.1190	62.940	28.36
0.95	3.9062	-	4.1247	62.939	49.47
0.975	3.9034	-	4.1434	63.133	62.30

3.8 Unit Cell Volume and Phase Separation in (1-x)BCN-(x)PT Compositions

To perceive the phenomenon of phase coexistence and phase separation in (1-x)BCN-(x)PT solid solution, the unit cell volumes of the two end components have to be taken into account. The unit cell volumes of two coexisting phases and their differences have been plotted as a function of composition in Fig 3.12(a) and Fig 3.12(b), respectively. The unit cell volume of the cubic phase 'C_1' decreases rapidly with increasing PT concentration from the 0.05 to 0.55 compositions, as shown in the inset figure of Fig 3.12(a). In the composition range $0.55 \leq x \leq 0.65$, the decrement rate reduces considerably. Phase 2 exhibits a gradually decreasing trend of the unit cell volume for the composition range $0.55 \leq x \leq 0.95$, followed by a slight increase in the 0.975 composition. However, the unit cell volume of phase 3 decreases with increasing PT concentration from the 0.70 to 0.80 compositions and then shows a continuously increasing trend up to the 0.975 composition. The small, yet noticeable, rise in the unit cell volume of the crystal structure of some compositions, viz., 0.60 and 0.70, may be attributed to the structural instabilities/flexibilities of the particular phases while varying the compositions, as there is a gradual evolution of different crystal structures with changing composition. In solid solutions consisting of MPBs, similar structural instabilities near phase boundaries and softening of the crystal structure can be seen as a result of the rotation of unit cell polarization [83,84]. As shown in Fig 3.12(b), a huge difference in the unit cell volume of the two coexisting phases is observed for the intermediate composition range from 0.70 to 0.85, which causes the phase separation phenomenon between the phase 1 and phase 2. The unit cell volumes of the two coexisting phases differ only slightly for the 0.59, 0.60, 0.62, 0.65, 0.90, 0.95 and 0.975 compositions, but there is a well-defined phase separation for the compositions in the range 0.70 ≤ x ≤ 0.85. Interestingly, in these compositions, one constituent phase exhibits monoclinic symmetry. The 0.80 composition has the largest unit cell volume difference for the coexisting phases.

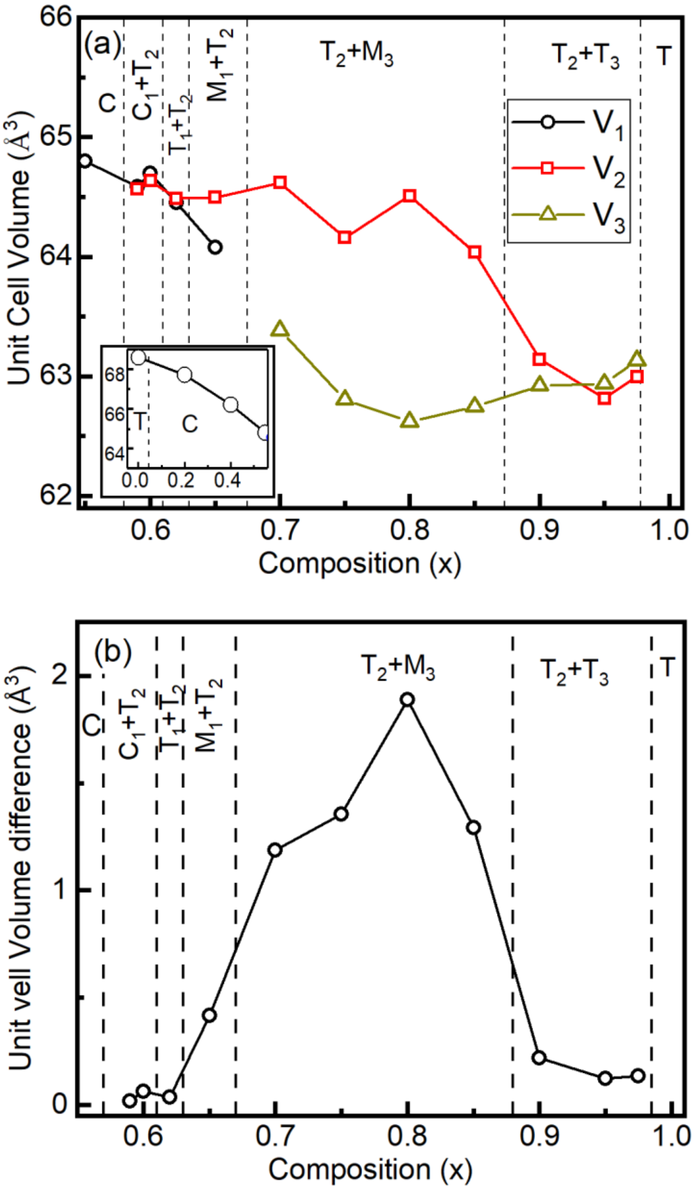

Fig 3.12 Composition-dependence of (a) unit cell volumes of different phases; (b) Difference in unit cell volume of coexisting phases in various compositions of (1-x)BCN-(x)PT ceramics

All the compositions, starting from 0.59 to 0.975, exhibit two coexisting crystallographic structures with variable degrees of phase separation, as manifested in the unit cell volume difference. The nature of the kind of phase coexistence in the compositions having large phase separation is discussed in detail in the next chapter. A subsequent study of the evolution of the crystal structure above room temperature to cryogenic temperatures, and the construction of a phase diagram of the solid solution, is also addressed in chapter 4.

3.9 Conclusions

The crystal structure for several compositions of a new solid solution (1-x)BCN-(x)PT, have been investigated with the help of Rietveld structural analysis of the XRD patterns at room temperature. Both, the BCN and PT perovskites, possess tetragonal symmetry and form a complete soluble solid solution in the entire composition range. Many distinct types of phase coexistence combinations comprising different crystal structure symmetries are observed in the composition range $0.59 \leq x \leq 0.975$. The solid solution exhibits, a cubic structure with *Pm*-3*m* space group for $0.05 \leq x \leq 0.55$ composition range, a coexistence of cubic and tetragonal structures having '*Pm*-3*m* + *P*4*mm*' space group combination in the composition range $0.59 \leq x < 0.62$, a coexistence of two tetragonal structures with '*P*4*mm* + *P*4*mm*' space group combination in the composition range $0.62 \leq x < 0.65$, a coexistence of monoclinic and tetragonal structures with '*Pm*+ *P*4*mm*' space group combination in the composition range $0.65 \leq x \leq 0.85$, a coexistence of two tetragonal structures with '*P*4*mm* + *P*4*mm*' space group combination in the composition range $0.90 \leq x < 0.975$ and finally the tetragonal structure with '*P*4*mm*' space group for further increasing $PbTiO_3$ concentration. These distinct phase combinations of different crystal structures, result in seven phase boundaries, for the solid solution with varying composition. The presence of multiple phase boundaries in the solid solution itself creates an excellent opportunity for discovering new phase transition behaviour and outstanding dielectric, ferroelectric and piezoelectric responses close to them.